Chemical Engineering Journal 452 (2023) 139321

Contents lists available at ScienceDirect

Chemical Engineering Journal

journal homepage: www.elsevier.com/locate/cej

Activate whole-body passivation ability of small isomeric D-π-A molecules via amino position effect to improve the photovoltaic performance of perovskite solar cells

Zonghan Guo [a,b], Tongxin Xue [a,b], Xiaoxu Sun [c], Dan Li [a,b], Fengyou Wang [a,b], Lin Fan [a,b], Xiaoyan Liu [a,b], Lili Yang [a,b,*], Maobin Wei [a,b,*]

[a] Key Laboratory of Functional Materials Physics and Chemistry of the Ministry of Education, Jilin Normal University, Changchun 130103, PR China
[b] National Demonstration Center for Experimental Physics Education, Jilin Normal University, Siping 136000, PR China
[c] Changchun Institute of Optics, Fine Mechanics and Physics, Chinese Academy of Sciences, Changchun 130033, PR China

ARTICLE INFO

Keywords:
Perovskite solar cells
Defect passivation
Group position effect
Photovoltaic performance

ABSTRACT

Passivating defects via organic molecule additives is one of important approaches to achieve high-efficient and stable perovskite solar cells (PSCs). To unveil the influence mechanism of intermolecular charge transfer caused by molecular structure on defect passivation is imperative for activating whole-body passivation ability of molecules. Small isomeric D-π-A molecules of methyl 2-amino-4-methoxybenzoate (M2A4M) and methyl 3-amino-4-methoxybenzoate (M3A4M) with multiple coordination sites provide us a desired research object to unveil how the intermolecular charge transfer caused by amino group position activate the passivation ability of molecule to boost the photovoltaic performance of PSCs. The results show that the *ortho* amino group within M2A4M is beneficial for part of electrons at $–CH_3O$ transferring to the methoxy and amino groups through benzene ring to activate their whole-body coordination ability with MA^+ or Pb related defects. In detail, a unique bidentate chelating bond between M2A4M and uncoordinated Pb^{2+} ions in the perovskite can be formed due to a good distance match between functional groups on M2A4M and adjacent octahedral voids on the perovskite caused by *ortho* amino group, which provides the stronger adsorption capacity to anchor M2A4M on the perovskite to passivate internal defects. Moreover, the formation of hydrogen bond between activated methoxy group in M2A4M and NH_3^+ in the perovskite can inhibit the ion migration to improve the stability of PSCs. As a result, the champion $MAPbI_3$ based PSCs treated with M2A4M achieves the highest photoelectric conversion efficiency of 21.51 % with an open circuit voltage of 1.16 V. This work provides a novel concept for designing appropriate molecular structure of additives with whole-body defect passivation ability, which will prompt the further development of perovskite-based photoelectric devices.

1. Introduction

Organic-inorganic hybrid perovskite solar cells (PSCs) keep attracting global attention considering its low-temperature manufacturing technology, large-area production capacity and relatively low cost. So far, the photoelectric conversion efficiency (PCE) of PSCs has risen rapidly from the initial 3.8 % in 2009 to 25.8 % in 2021 [1]. Such rapid development of PSCs depends on the excellent photoelectric properties of perovskite materials, including adjustable bandgaps, carrier diffusion length up to 1 μm, higher carrier mobility and higher light absorption coefficient of $\sim 10^5\ M^{-1}\ cm^{-1}$ [2]. In terms of current progress, it is no doubt that PSCs have turned out to be one of most promising candidates for the next generation photovoltaics.

However, compared to the 25-year service life of silicon-based solar cells, the stability of PSCs is far short of commercial requirements, which is one of obstacles on their road to commercialization [3,4]. It is recognized that the instability of PSCs is caused by the ionic nature of perovskite itself, which weakens the resistance of PSCs to humidity, oxygen, light, temperature, electric field, and aging stress [5]. Plus, the low-temperature solution fabrication technique inevitably produces a

* Corresponding authors at: Key Laboratory of Functional Materials Physics and Chemistry of the Ministry of Education, Jilin Normal University, Changchun 130103, PR China.
E-mail addresses: llyang1980@126.com (L. Yang), jlsdzccw@126.com (M. Wei).

https://doi.org/10.1016/j.cej.2022.139321
Received 14 July 2022; Received in revised form 11 September 2022; Accepted 16 September 2022
Available online 21 September 2022

large number of halide vacancies and under-coordinated Pb^{2+} ions at the surface of crystal lattice and grain boundaries (GBs) of perovskite films [6]. The existence of these defects will lead to even worse stability and then further deteriorate the efficiency of PSCs, since they can not only cause serious carrier recombination, block the carrier diffusion and shorten the carrier lifetime, but also assist the ion migration to accelerate the decomposition of perovskite [7–9]. Thus, to passivate these defects is still very necessary for achieving high-efficient and stable PSCs. So far, lots of molecules such as aminobenzoic acid, phenylalanine and l-lysine have been chosen to fill in vacancies or fix interstitial atoms with specific functional groups by forming coordination with the under-coordinated Pb^{2+} ions or halide anions [10–12]. Besides defect passivation function, those molecules can also perform multiple functions to upgrade the photovoltaic performance of PSCs as follows: (1) Anchor the adjacent layer by means of intermolecular forces to optimize interface contact and serve as specific charge channels to accelerate the charge transfer. (2) Form energy level cascade to improve carrier extraction capability. (3) Act as a barrier to block internal minority carrier transport and ion migration as well as external water molecules and gold/silver atoms penetration. Obviously, the passivation molecular additives applying in PSCs tend to develop in the direction of more multifunction or unveil the detailed interaction between functional groups and defects. However, there are few comprehensive studies on the fundamental design rules of passivation molecules so far. Wang et al. investigated the effects of chemical environment of a functional group on the defect passivation and demonstrated that the theophylline with N—H and C═O in an optimal configuration is activated for defect passivation since the hydrogen-bond formation between N—H and I (iodine) assisted the primary C═O binding with the antisite Pb (lead) defect to maximize surface-defect binding [13]. Yang et al. systematically designed the structures of passivation molecular functional groups and reveal their passivation capability to perovskites [11]. Due to the complexity and diversity of molecular structures, there are still many problems in molecular design rules to be further addressed. How the intramolecular interaction between groups affects the passivation ability of perovskite is one of the key problems to be solved. Especially, how to activate the whole-body defect passivation ability of one molecule is even more important for designing new molecules.

Here we selected the small organic D-π-A molecule consisting of an electron donor, a π-spacer and an electron acceptor as additives to passivate the perovskite films, since they usually possess advantages such as simple and economical preparation technology, diversified structures and high molar absorption coefficient [11]. In particular, they possess effective intramolecular electron transfer, so that the electron density distribution can be easily tuned by adjusting their electron-donating or electron-withdrawing functional groups, the chemical environment of a functional group and the relative positions of functional groups within molecules. Moreover, the small organic D-π-A molecules are able to exert stronger defect passivation ability, since not only electron-donating or electron-withdrawing functional groups such as carboxyl or amine groups can passivate the charged defects via electrostatic interactions, but also the aromatic structure can reduce the neutral iodine related defects [11]. Therefore, small organic D-π-A molecule with these advantages provides us a desired research object to unveil the influence mechanism of intermolecular charge transfer caused by molecular structure change on defect passivation, which will be very helpful for discovering design rules of passivation molecules.

Herein, the isomer molecules of methyl 2-amino-4-methoxybenzoate (M2A4M) and methyl 3-amino-4-methoxybenzoate (M3A4M) (see Fig. 1) were utilized as additives to passivate perovskite for the first time. The reason for selecting M2A4M and M3A4M isomer molecules is described as following: (1) Both the C═O double bond on methyl formate and the amino group on the benzene ring have lone electron pairs, which are good electron donating groups to form coordination bonds with uncoordinated Pb^{2+} ions in perovskite; (2) The aromatic rings have good hydrophobicity, strong steric hindrance and rigidity, and can provide a charge transfer channel within molecules, which is possible to strengthen the coordination between functional groups and perovskite, exhibiting a highly potential to further improve charge transfer; (3) Two molecules are isomers of each other, and the only difference in structure is the position of the amino group on the benzene ring. The amino group is located at the *ortho* and *meta* position relative to ester group for M2A4M and M3A4M, respectively. It is well known that differences in molecular structure affect not only the π-electron cloud density of the system, which in turn affects the conjugation effect of the molecule, but also the photophysical and electrochemical properties of the molecule itself. Thus, M2A4M and M3A4M isomer molecules just provide us excellent objects to study the influence of the relative position of specific groups within the multidentate additive molecule on the defect passivation and then photovoltaic performance of PSCs. We systematically investigated the defect passivation effect of M2A4M and M3A4M isomer molecules on perovskites. The study found

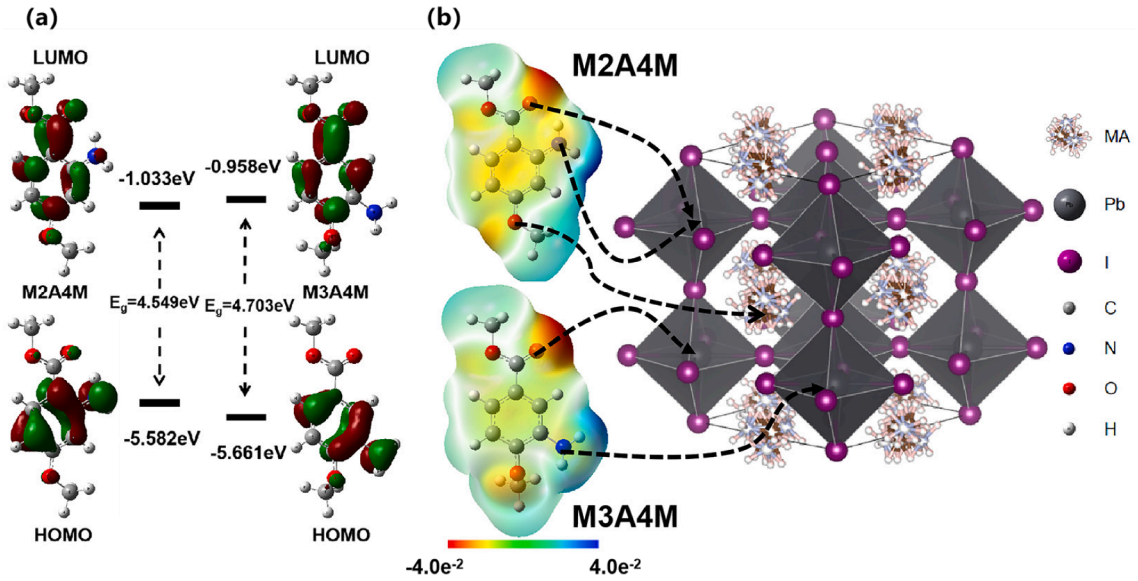

Fig. 1. DFT optimized molecular geometry, molecular frontier orbitals, calculated ESP profiles of M2A4M and M3A4M and schematic diagram of the functions of M2A4M and M3A4M on perovskite.

that both molecules can passivate the defects of perovskite, however, due to its excellent molecular configuration, M2A4M can make the amino group and C═O successfully form a chelate bond with Pb^{2+} ions in the perovskite at the same time, making it better anchored in the perovskite lattice. And the molecular structure with planarity can form better π-π conjugation, showing the most effective perovskite defect passivation effect. A maximum PCE of 21.51 % and larger V_{OC} of 1.16 V have been finally achieved in M2A4M modified $MAPbI_3$ based PSCs, and corresponding stability has also been significantly improved.

2. Experimental

Preparation of perovskite films: The 599.3 mg PbI_2 and 206.6 mg MAI were dissolved in a Dimethyl sulfoxide (DMSO) and Dimethylformide (DMF) mixed solvent (v:v = 3:7) to form a 1.3 M perovskite precursor solution. For M2A4M and M3A4M-based perovskite films, an additional 0.1–0.6 mg of M2A4M and M3A4M powders were added to the corresponding precursor solutions, respectively. We then spin-coat the precursor solution on the substrate in two steps, 500 rpm for 10 s and 4000 rpm for 30 s. In the second step, 450 μL of chlorobenzene (CB) was slowly dropped onto the substrate within 22 s, and then the process is completed.

The fabrication process of PSCs and characterization conditions are similar with our previous reports [14–18], which can be found in the supporting information.

3. Results and discussion

We firstly used density functional theory (DFT) to calculate the electrostatic potential (ESP) and the frontier molecular orbital of the M2A4M and M3A4M molecules to understand the electronic properties of the molecules and evaluate their possible interaction with the perovskite. The optimized molecular structure information is summarized in Table S1-4. The corresponding molecular structures and ESP maps are presented in Fig. 1 from which we can observe the charge distribution within both molecules. Through analyzing the variation of color gradient from blue to red in the ESP maps, the entire M2A4M molecule exhibits the stronger negative electric potential compared to M3A4M. Especially, the electron cloud densities at benzene rings, $–COOCH_3$ and $–NH_2$ groups within M2A4M apparently increase, indicating the $–NH_2$ groups located at *ortho*-position is beneficial for part of electrons at $–CH_3O$ transferring to the $–COOCH_3$ and $–NH_2$ groups through benzene ring [18]. Thus, these electron-rich $–COOCH_3$ and $–NH_2$ groups within M2A4M can play the role of Lewis base to coordinate with Pb related defects.

Meanwhile, the C═O and amino groups on M2A4M and M3A4M can simultaneously attack the positive charge center on the perovskite through electrostatic interaction, forming coordination bonds or coordination covalent bonds with uncoordinated Pb^{2+} ions. As shown in Figure S1, the distance difference between the distance from amino group to C═O (5.13 Å) within M3A4M and the distance of two adjacent Pb^{2+} ions (6.25 Å and 8.85 Å) on the perovskite is 1.12 Å and 3.72 Å. Such distance mismatch means that the amino group and C═O cannot coordinate with the adjacent Pb^{2+} ions at the same time, making M3A4M work only as a monodentate coordination body. On the contrary, the amino group on M2A4M is adjacent to C═O with a smaller distance of 2.69 Å, which provides M2A4M a chelating condition to make it work as a polydentate ligand, i.e. the amino group and C═O on M2A4M are apt to form a bidentate chelate bond with uncoordinated Pb^{2+} ions in the perovskite, which provides stronger adsorption capacity for the anchoring of M2A4M on the perovskite and passivates the interior defects of the perovskite [19]. These superior properties cannot be realized within M3A4M, since too long coordination distance is not conducive to its coordination with Pb^{2+} ions and the stacking of molecules [20]. These analysis results indicate that the M2A4M is promising to achieve a better defect passivation effect within perovskite films.

In order to study the electronic properties of M2A4M and M3A4M additives, we also analyzed their lowest unoccupied molecular orbital (LUMO) and highest occupied molecular orbital (HOMO). As shown in Fig. 1a, the LUMO and HOMO energy levels of M2A4M were calculated to be −1.033 eV and −5.582 eV, respectively, and the LUMO and HOMO energy levels of M3A4M were −0.958 eV and −5.661 eV, respectively. Moreover, it is worth to note that the LUMO of M2A4M and M3A4M are mainly concentrated on the benzene ring and methyl formate. But their HOMO are mainly concentrated on the amino and part of the benzene ring. Such obvious separation and partial overlap of HOMO and LUMO due to delocalization can reduce the intramolecular reorganization energy and increase the electronic coupling of adjacent molecules, which is conducive to the extraction and transportation of carrier [21]. Obviously, both molecules show a desired feature to achieve higher carrier transport.

Subsequently, a series of M2A4M and M3A4M based PSCs with different concentration were fabricated and corresponding *J-V* curves have been presented in Figure S2 and Figure S3. The corresponding photovoltaic parameters are summarized in Table S5 and Table S6, from which we can see that the highest PCE of M2A4M based PSCs has been achieved when the optimal concentration of M2A4M and M3A4M is 3.31 mM and 1.10 mM, respectively. Therefore, both M2A4M and M3A4M were incorporated into the perovskite precursor solution with their own optimized concentration in the following discussion. Fig. 2a and 2b illustrates the scanning electron microscope (SEM) and atomic force microscope (AFM) images of control, M2A4M and M3A4M based perovskite films. All perovskite films exhibit the flat and smooth morphologies. The average grain size distribution can be found in Figure S4. The average grain size of M2A4M and M3A4M increased from 268 nm to 400 nm and 290 nm, respectively. Compared to the control one, the average grain sizes of M2A4M and M3A4M based perovskite film turn larger. Since the coordination ability of M3A4M is weaker than that of M2A4M as proved by Fig. 1 and Figure S1, even though the grain size of M3A4M exhibits slightly increase compared to the control one, it is still smaller than that of M2A4M based one. Accordingly, the AFM images of control, M2A4M and M3A4M based perovskite films can be found in the Fig. 2b. The corresponding root-mean-square roughness (RMS) of three perovskite films can be determined to be 16.9, 10.6 and 15.3 nm, respectively. The obviously decreased RMS value in M2A4M based perovskite films will improve the interface contact between perovskite and hole transport layers (HTLs), which is beneficial for facilitating the top-down charge transfer process at the interface [22].

To further evaluate the effect of M2A4M and M3A4M on the crystal quality of perovskite films, Fig. 2c presents the X-ray diffraction (XRD) patterns of M2A4M and M3A4M based perovskite films. The diffraction peaks at 14.03°, 19.93°, 23.44°, 24.44°, 28.36°, 31.80°, 40.56°, 43.12° can be indexed to the (1 1 0), (1 1 2), (2 1 1), (2 0 2), (2 2 0), (2 2 2), (2 2 4) and (3 1 4) crystal planes, respectively, indicating the formation of perovskite with tetragonal structure [23]. Fig. 2d further shows the enlarged XRD patterns of (1 1 0) diffraction peak. We can see that the diffraction intensity of M2A4M and M3A4M based perovskite films turn slightly stronger and the M2A4M based one owns the strongest intensity, indicating the M2A4M based perovskite films possess the best crystal quality, which is consistent with the variation tendency of above SEM results. Fig. 2e further presents that the M2A4M based perovskite films own the smallest full-width half-maximum (FWHM), implying larger average grain size has been obtained [24]. Accordingly, M2A4M based perovskite films exhibit the strongest light harvesting capability due to their larger grain size and better crystal quality (Fig. 2f). Figure S5 shows the I-V curves of control, M2A4M and M3A4M based devices with ITO/perovskite/Ag structure to check the conductivity of perovskite films. The conductivity (σ_0) can be calculated by the following formula:

$$I=(\sigma_0 AV)/d \quad (1)$$

where A and d is the area of the sample (0.09 cm^2) and the thickness

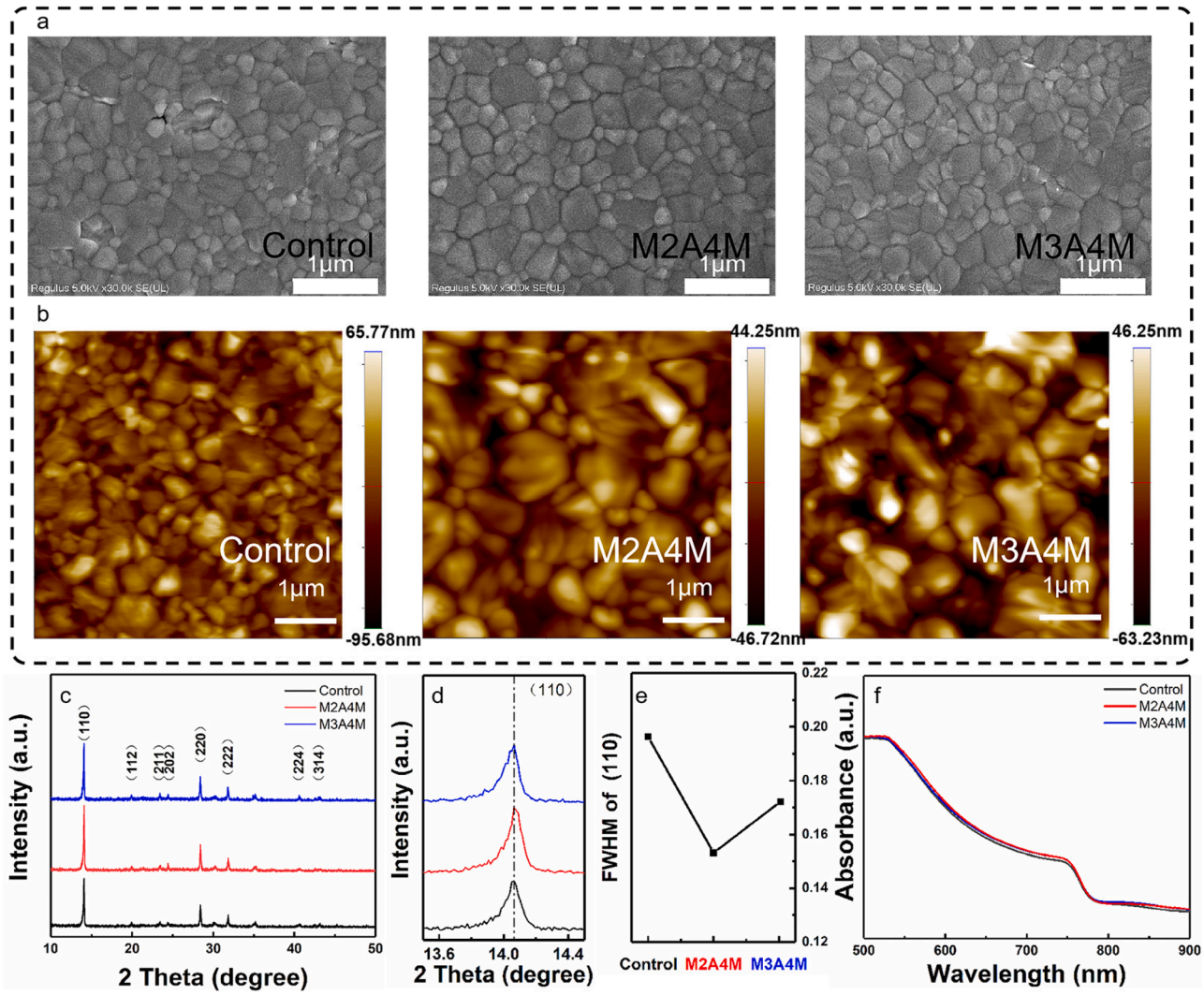

Fig. 2. Morphologies, crystal quality and absorption properties of control, M2A4M and M3A4M-based perovskite films. (a) top-view SEM images, (b) AFM images (c) XRD patterns, (d) Enlarged XRD patterns of (1 1 0) peaks (e) FWHM of (1 1 0) peaks (f) UV–visible spectra.

of the perovskite layer (~500 nm), respectively. The calculated conductivity of the control, M2A4M and M3A4M based perovskite films is 0.0318, 0.0358 and 0.0325 mS/cm, respectively. The strongest absorption ability and highest electron conductivity in M2A4M based perovskite films is very beneficial for achieving better photovoltaic performance in PSCs [25].

Generally, the chelation and hydrogen bonding between additives and perovskite are confirmed to play key role to reduce the critical Gibbs free energy of nucleation and slow down the growth of polycrystalline perovskite, which can be ascribed to the enlarged grain size perovskite films [22]. To reveal the interaction of M2A4M and M3A4M with perovskite, Fig. 3a and 3b show the FTIR spectra of M2A4M and M3A4M powders, control, M2A4M and M3A4M-based perovskite films. The peaks located at 1685 cm^{-1} and 1686 cm^{-1} in pure M2A4M and M3A4M powders are originated from typical C═O stretching vibration [26]. After introducing them into the perovskite film, we can find that the C═O stretching vibration peaks move to 1638 cm^{-1} and 1642 cm^{-1}, respectively. The reason is that the C═O can share the lone electron pairs to coordinate with free Pb^{2+} ions and lead to a decrease in electron cloud density, which will make the characteristic peak of C═O shift to lower wave numbers [27]. Moreover, we can see that the C═O peak shift in the M2A4M-based perovskite film (47 cm^{-1}) is larger than that of the M3A4M-based perovskite film (44 cm^{-1}), which might be attributed to the $–NH_2$ groups located at *ortho*-position within M2A4M providing more electrons for the C═O group, promoting its stronger interaction with Pb^{2+} ions [28]. In addition, the C—O—C asymmetric stretching vibration peaks of pure M2A4M and M3A4M are located at 1139 cm^{-1} and 1150 cm^{-1}, respectively. After introducing M2A4M into perovskite, the C—O—C peak shifted to 1150 cm^{-1}. Such large red-shift (11 cm^{-1}) of the C—O—C stretching vibration means that the bonding of C—O is reduced, which may be attributed to the interaction between the positively charged groups of the perovskite (such as Pb^{2+} ions) and the negatively charged O atoms of the additive molecules [29]. It is interesting to find that after introducing M3A4M into perovskite, no obvious shift happens in C—O—C peak, further proving the $–NH_2$ groups located at *ortho*-position within M2A4M provide more electrons for the C—O—C group to interact with perovsktite. From the magnified FTIR spectra of the 3000 ~ 3800 cm^{-1} region in Fig. 3c and 3d, it can be seen that the N—H asymmetric stretching oscillation peaks of pure M2A4M and M3A4M are located at 3465 cm^{-1} and 3452 cm^{-1}, respectively [30]. It shifts to 3448 cm^{-1} and 3446 cm^{-1} in the M2A4M and M3A4M-based perovskite films, respectively, indicating a chemical interaction between Pb and N in the perovskite. Meanwhile, the frequency shift for M2A4M-based perovskite films is larger than that of M3A4M-based perovskite films, indicating the M2A4M possesses a stronger coordination interaction between $–NH_2$ and Pb^{2+} ions. These results suggest that proper addition of M2A4M and M3A4M can delay the crystallization of perovskite and effectively terminate the subsurface defects of

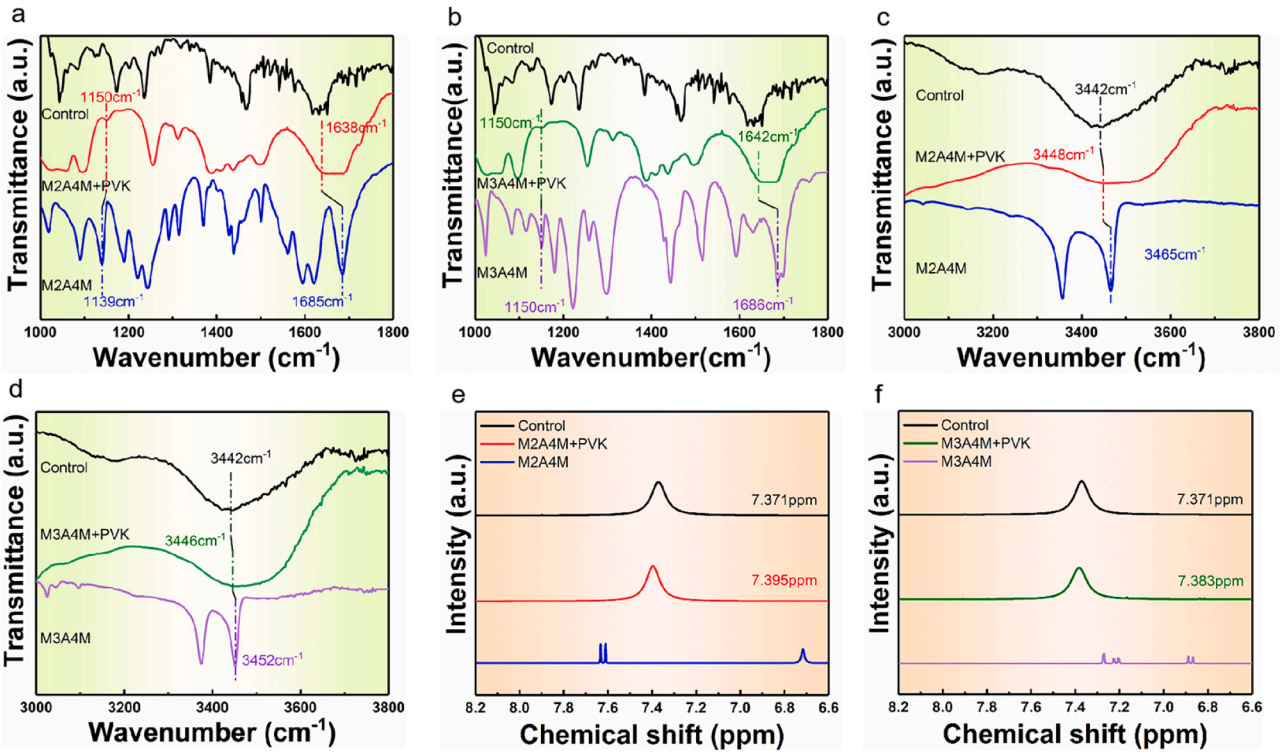

Fig. 3. (a-d) FTIR characterization of control precursor solution, pure additive powder and additive modified perovskite precursor solution, (e-f) ^{1}H NMR spectra of pure additive, $MAPbI_3$ with and without additive.

perovskite, resulting in the formation of high-quality perovskite films [31,32].

We further performed liquid nuclear magnetic resonance spectroscopy (NMR) to record the interaction between the additive and the perovskite. The ^{1}H NMR spectra of M2A4M, M3A4M, control, M2A4M and M3A4M based perovskite precursor solution are shown in Fig. 3e and 3f. The proton signal located at 7.37 ppm in the control perovskite film is originated from $–NH_3$ in MA. After introducing M2A4M and

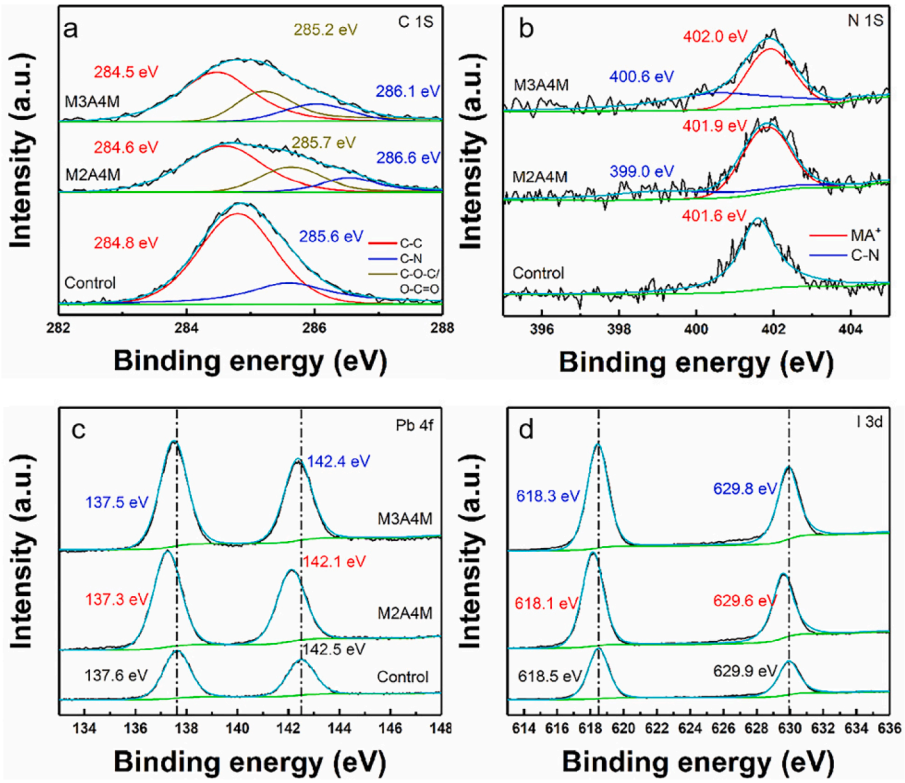

Fig. 4. XPS spectra of Control, M2A4M and M3A4M based perovskite films. (a) C 1s XPS spectra, (b) N 1s XPS spectra, (c) Pb 4f XPS spectra, (d) I 3d XPS spectra.

M3A4M, this peak moves to 7.39 and 7.38 ppm, respectively [22]. Obviously, compared to the M3A4M based perovskite film, the introduction of M2A4M caused more signal offset. The larger displacement of the proton signal further indicates that there is stronger hydrogen bonding between the NH_3 in the perovskite and the methoxy group in M2A4M [22]. The presence of hydrogen bond can immobilize MA^+, and prevent ion migration, thus delaying the decomposition of perovskite film [33]. In addition, we also analyzed the signal changes of organic molecules to testify the above results. In Figure S6, we can observe that the pure M2A4M and M3A4M exhibit the double peaks from $–NH_2$, which locates at 6.28 and 6.27 ppm, 6.89 and 6.87 ppm, respectively. After introducing them into perovskite, these signals shift to 6.22 and 6.21 ppm, 6.83 and 6.82 ppm, respectively [34]. This downfield shift of the $–NH_2$ signal in the mixture of additive and perovskite is mainly due to the deshielding effect of π electrons [35]. Moreover, the slight larger shift of M2A4M than that of M3A4M can be explained by the Brønsted-Lowry acid-base reaction [35]. Since the $–NH_2$ in M2A4M is adjacent to C═O, the intramolecular induction effect is stronger, which forces the methyl group to give more electrons to $–NH_2$ than that of M3A4M. Therefore, when $–NH_2$ interacts with the weak acid of ammonium group in MA, the $–NH_2$ signal of M2A4M exhibits a relative larger shift.

The X-ray photoelectron spectroscopy (XPS) measurements were further performed to achieve the information of the interaction of M2A4M and M3A4M with perovskite. All XPS spectra have been calibrated with the C 1s peak at 284.8 eV. The XPS survey spectra of control, M2A4M and M3A4M based perovskite films are shown in Figure S7, indicating the existence of C, N, O, Pb and I within three samples. Fig. 4a shows the corresponding C1s XPS spectra. As for the control perovskite film, the asymmetric C 1S XPS spectra can be well fitted by two Gaussian functions, indicating two kinds of carbon species exist in the samples. The peak at the lower binding energy of 284.8 eV is attributable to the C—C within perovskite film, while the peak located at the higher binding energy of 285.6 eV can be ascribed to the C—N in the CH_3NH_3 cation [36]. As for the M2A4M and M3A4M based perovskite films, three kinds of carbon species have been proved to be existed since three Gaussian functions are necessary for obtaining well-fitting curves for the asymmetric C 1S XPS spectra. Except for C—C and C—N peaks originated from perovskite, another characteristic peak appeared at 285.7 eV and 285.2 eV for M2A4M and M3A4M based perovskite films, respectively, which can be attributed to the C—O—C/O-C═O, indicating that both additives have been successfully introduced into the perovskite films [37]. After introducing M2A4M and M3A4M, no obvious change happens at the binding energy of C—C. But the binding energy of C—N shift to the higher energy of 286.6 eV and 286.1 eV for M2A4M and M3A4M based perovskite films in comparison with the control one (285.6 eV), respectively. Moreover, Fig. 4b shows the N 1s XPS spectra of control, M2A4M and M3A4M based perovskite films. For the control film, only one N 1s peak located at 401.6 eV can be observed, which is originated from $–CH_3NH_3$ [36]. After introducing M2A4M and M3A4M, asymmetric characteristics of N 1s XPS spectra occur, which can be deconvoluted into two peaks, indicating two nitrogen species exist in the M2A4M and M3A4M based perovskite films. The new N peaks at 399.0 eV and 400.6 eV can be assigned to the C—N bond of M2A4M and M3A4M molecular, respectively, further demonstrating the successful incorporation of the additive into the perovskite film [38].

The Pb 4f and I 3d core level XPS spectra are further shown in Fig. 4c and 4d to verify that the amino group and C═O coordinated with the uncoordinated Pb^{2+} ions. The binding energy of Pb 4f 7/2 and Pb 4f 5/2 of control sample is 137.6 eV and 142.5 eV, respectively. After introducing M2A4M and M3A4M, both Pb 4f 7/2 and Pb 4f 5/2 shift to the lower binding energy of 137.3 eV and 142.1 eV for M2A4M based perovskite film and 137.5 eV and 142.4 eV for M3A4M based perovskite film, respectively. Such reduction in binding energy is mainly caused by the increase of the electron cloud density of Pb ions due to the contribution of the lone pair electrons within M2A4M and M3A4M molecules [39]. Similarly, the I 3d core level XPS spectra in Fig. 4d also shifts toward lower binding energy after additive incorporation. These displacements indicate the interaction of coordination and hydrogen bond happens between additive molecules and perovskite. Moreover, the Pb 4f and I 3d shift of M3A4M-based perovskite films in contrast to control one are all less than that of M2A4M-based one, which further verifies that the interaction ability of M2A4M with perovskite was stronger than that of M3A4M.

Here we would like to present the O1s XPS spectra in Figure S8 to check the stability of perovskite films during the transport and measurement process. Two Gaussian functions are required to fit the curve of the control perovskites films, while three Gaussian functions are necessary to get good fitting curves for the M2A4M and M3A4M based perovskites films. All three perovskites show characteristic peaks of metal oxides and metal carbonates [37]. After introducing M2A4M and M3A4M, besides these two peaks, we can observe another peak located at 532.2 eV and 532.1 eV, which is originated from O-C═O of additives, which further indicating the cooperation of additives into perovskite films [40]. Obviously, the ratio of whole intensity of O 1s peak of Control: M2A4M: M3A4M is 2.19: 1: 2.03. It means that introducing M2A4M and M3A4M can suppress the degradation of perovskite films, and M2A4M based one is more stable than that of M3A4M-based one due to its stronger coordination ability.

Based on all above more apparent variation tendency caused by M2A4M molecule within crystal structure, chemical composition and theoretical calculation results, we can conclude that the M2A4M molecule with more optimized molecular configuration superiorly participate in the crystal growth process of perovskite films, not only amino group and C═O can coordinate with uncoordinated Pb^{2+} ions to passivate defects, but also the methoxy group can form a hydrogen bond with NH_3^+ in the perovskite to stabilize the organic cation and inhibit the ion migration, which well explains the improvement of crystal quality, absorption ability and conductivity and exhibits great potential to boost the photovoltaic performance of PSCs.

Subsequently, the control, M2A4M and M3A4M based PSCs were fabricated and corresponding forward and reverse scanning J-V curves under AM 1.5G illumination have been presented in Fig. 5a. The corresponding photovoltaic parameters have been summarized in Table S7. The reverse PCE of control, M2A4M and M3A4M based PSCs is 19.09 % ±0.36, 21.51 %±0.27 and 20.12 %±0.30, respectively. And corresponding hysteresis-index (HI) calculated via equation of HI (%) = $(PCE_{reverse} - PCE_{forward})/PCE_{reverse}$ is 14.88 %, 4.79 % and 9.69 %, respectively. Apparently, the M2A4M based PSCs exhibit the best photovoltaic performance and smallest hysteresis. Although the photovoltaic performance of M3A4M based PSCs is better than that of control device, it is still worse than that of M2A4M based PSCs, which is consistent with above analysis results. We further fabricate 20 devices for each PSCs and the corresponding distribution box diagrams of each photovoltaic parameter are shown in Figure S9, clearly proving that the improvement effects of M2A4M and M3A4M additives on PSCs are highly reproducible. Here we would like to point out that the average values of photovoltaic parameters are obtained accordingly, which is then used to evaluate the experimental error. The experimental error values of PCE in Fig. 5a were obtained by minus this average value and then divided by 2.

Furthermore, we can observe from Table S7 that the open circuit voltage (Voc), short current density (Jsc) and fill factor (FF) of M2A4M based PSCs significantly increased compared to the control one. Among them, the Jsc increases from 22.58 mA cm^{-2} of control device to 23.65 and 23.06 mA cm^{-2} for the M2A4M and M3A4M based PSCs, respectively. Accordingly, Fig. 5b shows the external quantum efficiency (EQE) spectra of three optimal devices. Both M2A4M and M3A4M based PSCs exhibit higher light response in the range of 380 ~ 750 nm than that of control device [41]. The integrated Jsc originated from EQE spectra of control, M2A4M and M3A4M based PSCs are 22.04, 23.15, and 22.83 mA cm^{-2}, respectively. The variation trend is well consistent with the data obtained from the J-V test and the error is within 5 % [42].

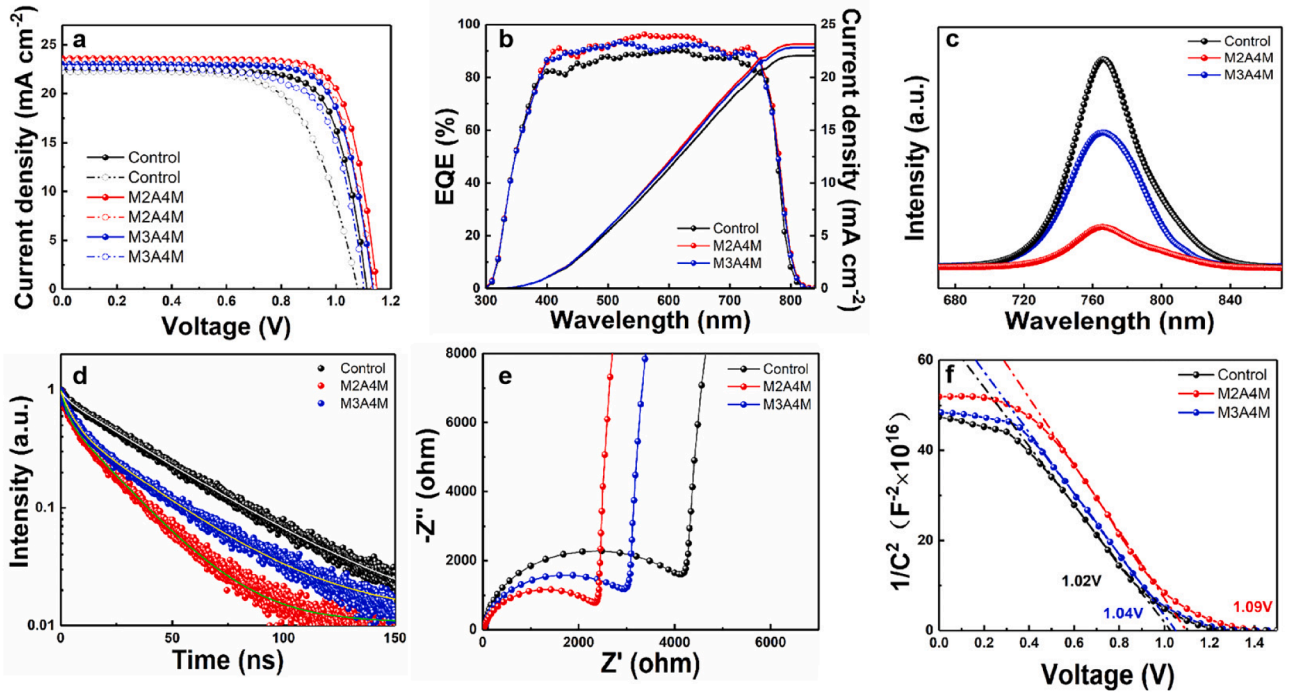

Fig. 5. Photovoltaic performance and charge transfer characterization of Control, M2A4M and M3A4M based PSCs. (a) J-V curves with forward and reverse scanning,(b) EQE spectra, (c) Steady-state PL spectra and (d) Time-resolved PL spectra of ITO/SnO_2/perovskite under 385 nm excitation, (e) Electrochemical impedance spectra, (f) Mott-Schottky curves.

Charge transfer is another important factor to determine the Jsc, Voc and then photovoltaic performance. The steady-state photoluminescence (PL) and time-resolved photoluminescence (TRPL) spectra of control, M2A4M and M3A4M perovskite on ITO/SnO_2 were shown in Fig. 5c and 5d. The strong PL quenching of M2A4M and M3A4M-based ones indicates the high-efficient carrier injection from perovskite into SnO_2 ELTs. As shown in Fig. 5d, a biexponential decay function with a fast decay (τ_1) and a low decay (τ_2) are used to obtain well-fitting curves for all TRPL spectra [43,44]. The τ_1 is related to the interfacial charge transfer and intensity quenching caused by defects, while τ_2 is related to the free carrier recombination. The corresponding fitting parameters are summarized in Table S8. Obviously, after introducing M2A4M and M3A4M, the average carrier lifetime decreases from 323.53 ns of control film to 203.44 and 303.03 ns, respectively. Both strong PL quenching and shorter carrier lifetime within M2A4M-based devices prove that the electron can be efficiently transfer to the electrode, and the charge accumulation and recombination can be effectively suppressed, which can increase the Jsc, Voc and suppress the hysteresis of PSCs [14].

To further investigate the effects of additives on the interface charge transfer process, electrical impedance spectroscopy (EIS) spectra of control, M2A4M and M3A4M based PSCs were show in Fig. 5e. The Nyquist plots showed a large arc at the high-frequency and a small arc at the low-frequency, which is related to the parameter of charge transport resistance (*R*tr) reflecting the charge transport features and recombination resistance (*R*rec) reflecting the charge recombination process at interface, respectively [24]. These Nyquist plots were fitted by the quivalent circuit diagram shown in Figure S10 and corresponding fitting parameters are shown in Table S9. Since three devices own the similar structure, their ohmic resistance (*Rs*) are similar. But both R_{tr} and R_{rec} have been significantly improved due to the addition of M2A4M and M3A4M, which proves that the charge extraction process has been improved and the charge recombination process has been suppressed, finally resulting in the improvement of FF and Voc.

Mott-Schottky test (MS) is another effective approach to characterize the charge transport behavior within PSCs via the following equation [45]:

$$1/C^2 = 2(V_{bi}\text{-}V)/\varepsilon\varepsilon_0 eA^2N \quad (2)$$

where *C*, *V* and *A* is the measured capacitance, bias and active area, respectively. ε_0, ε and e is the permittivity of free space, static permittivity and elementary charge, respectively. The *N* and V_{bi} is the carrier density and built-in potential in PSCs, respectively. According to Eq. (2), the carrier density at the perovskite interface can be extracted from the linear region of the plots, which can be determined by the slope of the Mott–Schottky plot via inversely proportional manner. After calculation on the Fig. 5f, the slope of control, M2A4M and M3A4M based PSCs is 1.089×10^{16} , 3.759×10^{16} and 1.285×10^{16}, respectively. Such obvious larger slope originated from M2A4M based device indicates the trap states density has been reduced, which in turn results in a suppressed nonradiative carrier recombination. In addition, the V_{bi} can be also extracted from the intercept of $1/C^2$ with the x-axis. The obtained V_{bi} for control, M2A4M and M3A4M based PSCs is 1.02, 1.09 and 1.04 V, respectively. The higher V_{bi} in M2A4M-based devices provides a stronger driving force for charge separation, transport, and extraction [46].

Then we use the light intensity-related Voc curve to evaluate the effect of trap-assisted recombination on the device (Fig. 6a). Under open circuit conditions, Voc can be described by [47]:

$$Voc = nkTln\{(J_{ph}/J_0) + 1\}/q \quad (3)$$

where n is an ideal factor representing the recombination rate of charge carriers, *k* is Boltzmann's constant, *T* is temperature, J_{ph} is the photocurrent density, and J_0 is the reverse saturation current density. The trap-assisted recombination in PSCs can be evaluated from the deviation of the slope from unity *kT/q*. After fitting, the slope of control, M2A4M and M3A4M based PSCs is 1.74*KT/q*, 1.31*KT/q* and 1.53*KT/q*, respectively [48]. According to Eq. (3), the smaller n value of M2A4M based device further proves that the trap assisted recombination is lower than other two devices. Moreover, the longest carrier life within M2A4M based device appeared in the transient photo voltage (TPV) spectra in Fig. 6b also verifies that the addition of M2A4M greatly prevents the charge recombination. The less leakage current shown in the dark J-V

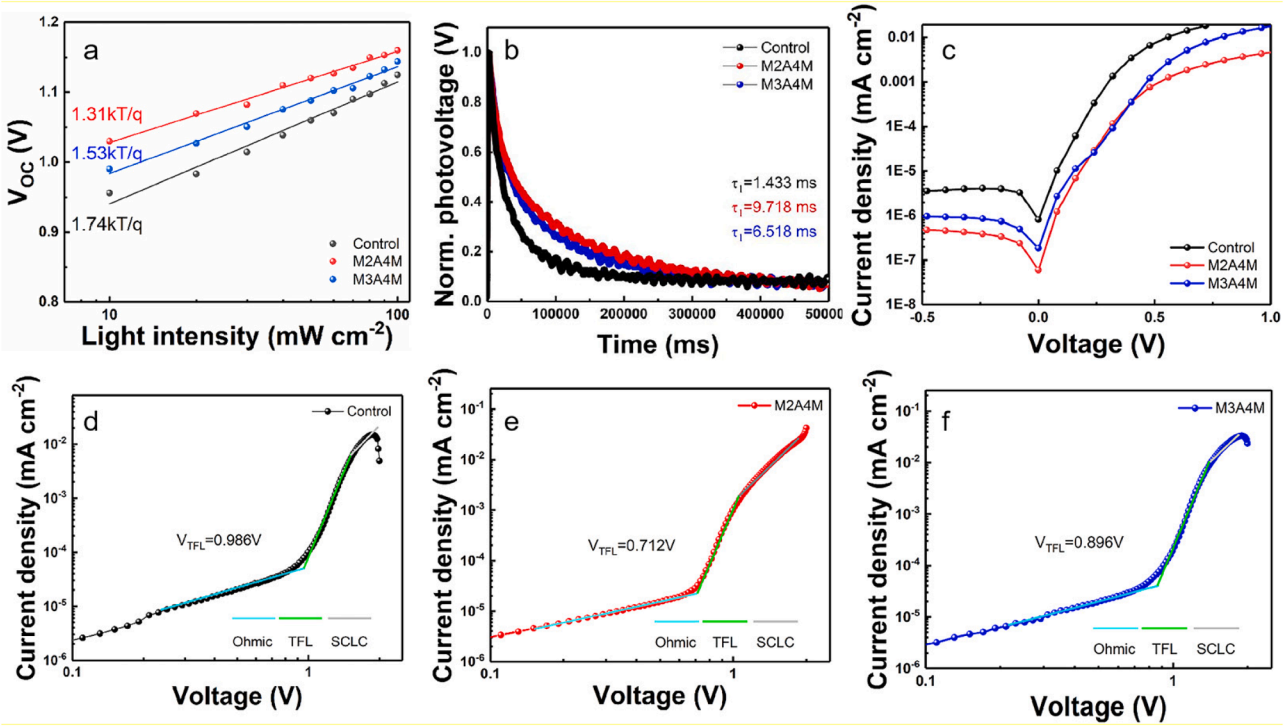

Fig. 6. (a) Dependence of Voc on light density, (b) TPV spectra of Control, M2A4M and M3A4M based PSCs, (c) Dark current density of Control, M2A4M and M3A4M based PSCs, (d-f) Dark current curves of pure electronic devices with ITO/SnO_2/$MAPbI_3$/PCBM/Ag architecture for control, M2A4M and M3A4M based perovskite films.

curves in Fig. 6c further proves this result.

Subsequently, it is necessary for us to fabricate electron-only devices with architecture of ITO/SnO_2/perovskite/PCBM/Ag to quantitatively calculate the trap state density using the space charge limited current (SCLC) method. The trap state density (N_t) can be determined by the V_{TFL} using the equation [49–51]:

$$N_t = 2\varepsilon_0\varepsilon_r V_{TFL}/eL^2 \quad (4)$$

where e is the unit charge, L is the thickness of the film, and ε_0 is the vacuum permittivity, ε_r is the relative dielectric constant of perovskite, respectively. It is well known that the trap density levels are continuously filled in the trap-filled limited region, and all the traps are filled until trap-filled limit voltage (V_{TFL}) as bias increases [52]. According to the V_{TFL} values in Fig. 6d-f, the defect density of the control, M2A4M and M3A4M based perovskite films is estimated to be 9.86 × 10^{15}, 7.12 × 10^{15}, and 8.96 × 10^{15} cm^{-3}, respectively. Such variation trend is well consistent with above reduced charge recombination within M2A4M based PSCs due to the stronger coordinating ability of M2A4M with Pb^{2+} ions.

Band alignment within PSCs is very important factor to determine the interface charge transfer process. Therefore, we used the ultraviolet photoelectron spectroscopy (UPS) to probe the work function, conduction band minimum (CBM) and valence band maximum (VBM) of the additive modified perovskite. As shown in the secondary electron region on the left side of Figure S11, the work functions of control, M2A4M and M3A4M modified perovskites can be determined to all be 4.30 eV. The VBM is determined by the valence band region on the right, which is all 1.34 eV. The band gaps obtained via Tauc plot of the control, M2A4M and M3A4M based perovskites in Figure S12 are 1.61, 1.60 and 1.60 eV, respectively. Obviously, the introduction of additives did not bring obvious change in energy band alignment due to the slight addition amount. Thus, the increase of Voc should be mainly attributed to the effective defects reduction and suppression of carrier recombination within PSCs [53].

Finally, the operational stabilities of control, M2A4M and M3A4M based devices were examined under maximum power point voltage (V_{mpp}) tracking, respectively (Fig. 7a). After continuous illumination for 250 s, the champion control, M2A4M and M3A4M based devices show a steady *PCE* of 14.26 %±0.34, 20.06 %±0.25 and 18.47 %±0.31, respectively. The improved performance of M2A4M-based PSCs can be attributed to the passivation of defects in perovskite films by M2A4M and the efficient charge transfer, resulting in the higher Jsc, Voc and FF to achieve higher PCE. Moreover, Fig. 7b shows the corresponding long-term stability of the unencapsulated PSCs under atmosphere and relative humidity of about 45 %. Apparently, the PCE of the unpackaged M2A4M based device can still maintain 90 % of the initial efficiency after 30 days, while the control and M3A4M based device can only maintain 70 % and 60 %, respectively. The improved stability of the M2A4M based devices can be ascribed to both the good crystal quality of perovskite films with low defect density and the formation of hydrogen bond between methoxy group in M2A4M and NH_3^+ in the perovskite to inhibit the ion migration. Meanwhile, since M2A4M and M3A4M owns good hydrophobicity, the water contact angle of the obtained M2A4M and M3A4M based perovskite films also obviously increased (Fig. 7c), which can effectively prevent water infiltration into perovskite and improve the stability of PSCs.

4. Conclusions

In summary, we systematically investigated the amino group position effects within small isomeric D-π-A molecules of M2A4M and M3A4M on defect passivation and photovoltaic performance of PSCs via intermolecular charge transfer. Three advantages have been proved for –NH_2 groups locating at *ortho*-position to boost the photovoltaic performance of PSCs. Firstly, the ESP calculation results unveil that the –NH_2 groups locating at *ortho*-position within M2A4M enhance the electron cloud density around the –$COOCH_3$ and –NH_2 groups due to the electron transfer from –CH_3O through benzene ring, so that improves the coordination ability of M2A4M. Secondly, from the view of molecule

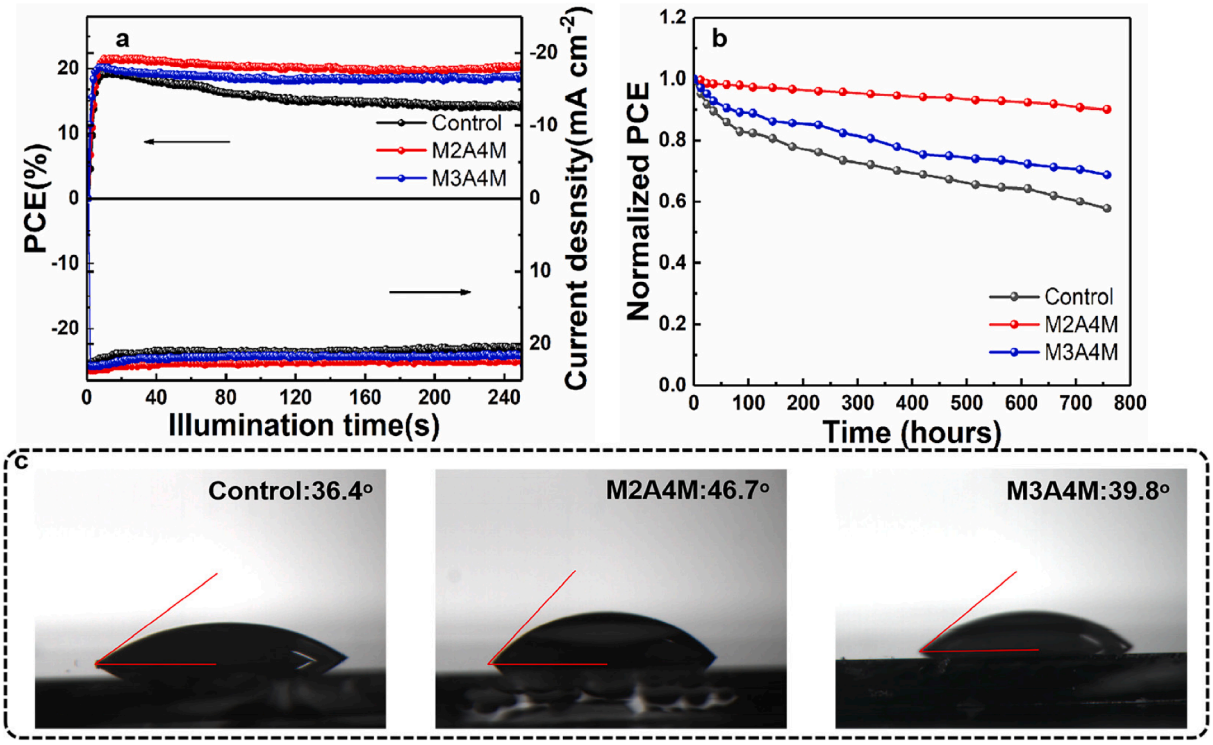

Fig. 7. (a) MPP and (b) PCE attenuation in an air environment with a relative humidity of 45%, (c) Water contact angles.

structure, due to the lactation of $–NH_2$ at *ortho*-position, the distance from $–NH_2$ to C═O within M2A4M molecular matches well with the distance between the adjacent octahedral voids in the perovskite, so that M2A4M can possess much stronger adsorption capacity to anchor themselves on the perovskite and passivate the internal defects of perovskite due to the formation of a unique bidentate chelating bond between M2A4M and uncoordinated Pb^{2+} ions in the perovskite. Finally, the formation of hydrogen bond between methoxy group in M2A4M and NH_3^+ in the perovskite can further inhibit the ion migration and improve the stability of PSCs. The first two advantages cannot be achieved in the M3A4M molecules, convincingly proving the importance of relative position of $–NH_2$ group within small D-π-A molecules. Finally, the champion $MAPbI_3$ based PSCs treated with M2A4M achieved the highest PCE of 21.51 % with a larger Voc of 1.16 V. This work enriches the design rules of additive molecules and provides theoretical and experimental references for developing new additive molecules to overcome bottlenecks of perovskite photoelectric devices in the future.

Declaration of Competing Interest

The authors declare that they have no known competing financial interests or personal relationships that could have appeared to influence the work reported in this paper.

Data availability

No data was used for the research described in the article.

Acknowledgements

The authors would like to acknowledge financial support for this work from National Nature Science Foundation of China (Grant Nos. 22075101, 61904066, 11904127), Program for the development of Science and Technology of Jilin province (Item No. 20200801032GH, 20210509050RQ, 20210101410JC), the Thirteenth Five-Year Program for Science and Technology of Education Department of Jilin Province (Item No. JJKH20210440KJ, JJKH20200417KJ).

Appendix A. Supplementary data

Supplementary data to this article can be found online at https://doi.org/10.1016/j.cej.2022.139321.

References

[1] H. Min, D.Y. Lee, J. Kim, G. Kim, K.S. Lee, J. Kim, M.J. Paik, Y.K. Kim, K.S. Kim, M. G. Kim, Perovskite solar cells with atomically coherent interlayers on SnO_2 electrodes, Nature 598 (7881) (2021) 444–450.
[2] M. Cai, Y. Wu, H. Chen, X. Yang, Y. Qiang, L. Han, Cost-performance analysis of perovskite solar modules, Advanced Science 4 (1) (2017) 1600269.
[3] K. Yao, S. Li, Z. Liu, Y. Ying, P. Dvorak, L. Fei, T. Sikola, H. Huang, P. Nordlander, A.K. Jen, D. Lei, Plasmon-induced trap filling at grain boundaries in perovskite solar cells, Light: Science & Applications 10 (1) (2021) 219.
[4] B. Wang, H. Li, Q. Dai, M. Zhang, Z. Zou, J.L. Bredas, Z. Lin, Robust Molecular Dipole-Enabled Defect Passivation and Control of Energy-Level Alignment for High-Efficiency Perovskite Solar Cells, Angew Chem Int Ed Engl 60 (32) (2021) 17664–17670.
[5] T. Leijtens, G.E. Eperon, N.K. Noel, S.N. Habisreutinger, A. Petrozza, H.J. Snaith, Stability of metal halide perovskite solar cells, Advanced Energy Materials 5 (20) (2015) 1500963.
[6] J. You, Z. Hong, Y. Yang, Q. Chen, M. Cai, T.B. Song, C.C. Chen, S. Lu, Y. Liu, H. Zhou, Low-temperature solution-processed perovskite solar cells with high efficiency and flexibility, ACS nano 8 (2) (2014) 1674–1680.
[7] M. Zhang, M. Ye, W. Wang, C. Ma, S. Wang, Q. Liu, T. Lian, J. Huang, Z. Lin, Synergistic Cascade Carrier Extraction via Dual Interfacial Positioning of Ambipolar Black Phosphorene for High-Efficiency Perovskite Solar Cells, Advanced Materials 32 (28) (2020) e2000999.
[8] Z. Chen, M. Segev, Highlighting photonics: looking into the next decade, eLight 1 (1) (2021) 2.
[9] S. Liang, M. Zhang, G.M. Biesold, W. Choi, Y. He, Z. Li, D. Shen, Z. Lin, Recent Advances in Synthesis, Properties, and Applications of Metal Halide Perovskite Nanocrystals/Polymer Nanocomposites, Advanced Materials 33 (50) (2021) e2005888.
[10] T. Zhang, H. Li, S. Liu, X. Wang, X. Gong, Q. Sun, Y. Shen, M. Wang, Low-temperature stable α-phase inorganic perovskite compounds via crystal cross-linking, The Journal of Physical Chemistry Letters 10 (2) (2018) 200–205.
[11] S. Yang, J. Dai, Z. Yu, Y. Shao, Y. Zhou, X. Xiao, X.C. Zeng, J. Huang, Tailoring passivation molecular structures for extremely small open-circuit voltage loss in perovskite solar cells, Journal of the American Chemical Society 141 (14) (2019) 5781–5787.

[12] W. Zhang, X. Liu, B. He, J. Zhu, X. Li, K. Shen, H. Chen, Y. Duan, Q. Tang, Enhanced efficiency of air-stable CsPbBr 3 perovskite solar cells by defect dual passivation and grain size enlargement with a multifunctional additive, ACS Applied Materials & Interfaces 12 (32) (2020) 36092–36101.

[13] R. Wang, J. Xue, K.L. Wang, Z.K. Wang, Y. Luo, D. Fenning, G. Xu, S. Nuryyeva, T. Huang, Y. Zhao, Constructive molecular configurations for surface-defect passivation of perovskite photovoltaics, Science 366 (6472) (2019) 1509–1513.

[14] Z. Lv, L. He, H. Jiang, X. Ma, F. Wang, L. Fan, M. Wei, J. Yang, L. Yang, N. Yang, Diluted-CdS quantum dot-assisted SnO_2 electron transport layer with excellent conductivity and suitable band alignment for high-performance planar perovskite solar cells, ACS Applied Materials & Interfaces 13 (14) (2021) 16326–16335.

[15] Y. Sun, Z. Pang, Y. Quan, D. Han, X. Zhang, X. Ge, F. Wang, Y. Sun, J. Yang, L. Yang, A synchronous defect passivation strategy for constructing high-performance and stable planar perovskite solar cells, Chemical Engineering Journal 413 (2021), 127387.

[16] L. He, Z. Lv, H. Jiang, X. Ma, F. Wang, L. Fan, M. Wei, J. Yang, L. Yang, H. Liu, Sandwich-like electron transporting layer to achieve highly efficient perovskite solar cells, Journal of Power Sources 453 (2020), 227876.

[17] Z. Pang, Y. Sun, Y. Gao, X. Zhang, Y. Sun, J. Yang, F. Wang, L. Yang, Unravelling the mechanism of interface passivation engineering for achieving high-efficient ZnO-based planar perovskite solar cells, Journal of Power Sources 438 (2019), 226957.

[18] H. Jiang, X. Qu, L. He, Z. Lv, D. Li, F. Wang, L. Fan, J. Yang, L. Yang, Y. Yan, A design strategy of additive molecule for PSCs: anchoring intrinsic properties of functional groups by suppressing long-range conjugation effect, Chemical Engineering Journal 427 (2022), 131676.

[19] S. Fu, X. Li, L. Wan, Y. Wu, W. Zhang, Y. Wang, Q. Bao, J. Fang, Efficient passivation with lead pyridine-2-carboxylic for high-performance and stable perovskite solar cells, Advanced Energy Materials 9 (35) (2019) 1901852.

[20] C. Liu, Y. Yang, K. Rakstys, A. Mahata, M. Franckevicius, E. Mosconi, R. Skackauskaite, B. Ding, K.G. Brooks, O.J. Usiobo, Tuning structural isomers of phenylenediammonium to afford efficient and stable perovskite solar cells and modules, Nature communications 12 (1) (2021) 1–9.

[21] K. Sun, X. Tang, Y. Ran, R. He, W. Shen, M. Li, π-Bridge modification of thiazole-bridged DPP polymers for high performance near-IR OSCs, Physical Chemistry Chemical Physics 20 (3) (2018) 1664–1672.

[22] S. Xiong, T. Hao, Y. Sun, J. Yang, R. Ma, J. Wang, S. Gong, X. Liu, L. Ding, M. Fahlman, Defect passivation by nontoxic biomaterial yields 21% efficiency perovskite solar cells, Journal of Energy, Chemistry 55 (2021) 265–271.

[23] P. Zhang, F. Yang, G. Kapil, C.H. Ng, T. Ma, S. Hayase, Preparation of perovskite films under liquid nitrogen atmosphere for high efficiency perovskite solar cells, ACS Sustainable Chemistry & Engineering 7 (4) (2019) 3956–3961.

[24] F. Wang, M. Yang, Y. Zhang, L. Yang, L. Fan, S. Lv, X. Liu, D. Han, J. Yang, Activating old materials with new architecture: boosting performance of perovskite solar cells with H_2O-assisted hierarchical electron transporting layers, Advanced Science 6 (4) (2019) 1801170.

[25] J.H. Heo, K. Im, H.J. Lee, J. Kim, S.H. Im, Ni, Ti-co-doped MoO_2 nanoparticles with high stability and improved conductivity for hole transporting material in planar metal halide perovskite solar cells, Journal of Industrial and Engineering Chemistry 94 (2021) 376–383.

[26] S. Fu, J. Wang, X. Liu, H. Yuan, Z. Xu, Y. Long, J. Zhang, L. Huang, Z. Hu, Y. Zhu, Multifunctional liquid additive strategy for highly efficient and stable $CsPbI_2Br$ all-inorganic perovskite solar cells, Chemical Engineering Journal 422 (2021) 130572.

[27] M. Luo, X. Zong, W. Zhang, M. Hua, Z. Sun, M. Liang, S. Xue, A Multifunctional Fluorinated Polymer Enabling Efficient $MAPbI_3$-Based Inverted Perovskite Solar Cells, ACS Appl Mater Interfaces 14 (27) (2022) 31285–31295.

[28] Q. Zhuang, C. Zhang, C. Gong, H. Li, H. Li, Z. Zhang, H. Yang, J. Chen, Z. Zang, Tailoring multifunctional anion modifiers to modulate interfacial chemical interactions for efficient and stable perovskite solar cells, Nano Energy 102 (2022) 107747.

[29] J. Xiong, N. Eedugurala, Y. Qi, W. Liu, A.R. Benasco, Q. Zhang, S.E. Morgan, M. D. Blanton, J.D. Azoulay, Q. Dai, Efficient and stable perovskite solar cells via shortwave infrared polymer passivation, Solar Energy Materials and Solar Cells 220 (2021), 110862.

[30] F. Wang, X. Li, J. Du, H. Duan, H. Wang, Y. Gou, L. Yang, L. Fan, J. Yang, F. Rosei, Coordinating light management and advance metal nitride interlayer enables $MAPbI_3$ solar cells with> 21.8% efficiency, Nano Energy 92 (2022), 106765.

[31] L.L. Jiang, Z.K. Wang, M. Li, C.C. Zhang, Q.Q. Ye, K.H. Hu, D.Z. Lu, P.F. Fang, L. S. Liao, Passivated perovskite crystallization via g-C_3N_4 for high-performance solar cells, Advanced Functional Materials 28 (7) (2018) 1705875.

[32] J. Colaux, P. Louette, G. Terwagne, XPS and NRA depth profiling of nitrogen and carbon simultaneously implanted into copper to synthesize C_3N_4 like compounds, Nuclear Instruments and Methods in Physics Research Section B: Beam Interactions with Materials and Atoms 267 (8–9) (2009) 1299–1302.

[33] T. Li, S. Wang, J. Yang, X. Pu, B. Gao, Z. He, Q. Cao, J. Han, X. Li, Multiple functional groups synergistically improve the performance of inverted planar perovskite solar cells, Nano Energy 82 (2021), 105742.

[34] R. Satheeshkumar, K. Prabha, K.N. Vennila, K. Sayin, E. Güney, W. Kaminsky, R. Acevedo, Spectroscopic (FT-IR, NMR, single crystal XRD) and DFT studies including FMO, Mulliken charges, and Hirshfeld surface analysis, molecular docking and ADME analyses of 2-amino-4′-fluorobenzophenone (FAB), Journal of Molecular Structure 1267 (2022) 133552.

[35] H. Kim, J.S. Kim, J.M. Heo, M. Pei, I.H. Park, Z. Liu, H.J. Yun, M.H. Park, S. H. Jeong, Y.H. Kim, J.W. Park, E. Oveisi, S. Nagane, A. Sadhanala, L. Zhang, J. J. Kweon, S.K. Lee, H. Yang, H.M. Jang, R.H. Friend, K.P. Loh, M.K. Nazeeruddin, N.G. Park, T.W. Lee, Proton-transfer-induced 3D/2D hybrid perovskites suppress ion migration and reduce luminance overshoot, Nature communications 11 (1) (2020) 3378.

[36] T.J. Jacobsson, J.-P. Correa-Baena, E. Halvani Anaraki, B. Philippe, S.D. Stranks, M.E. Bouduban, W. Tress, K. Schenk, J.l. Teuscher, J.-E. Moser, Unreacted PbI2 as a double-edged sword for enhancing the performance of perovskite solar cells, Journal of the American Chemical Society 138 (32) (2016) 10331–10343.

[37] Z. Ahmad, M.A. Najeeb, R. Shakoor, A. Alashraf, S.A. Al-Muhtaseb, A. Soliman, M. Nazeeruddin, Instability in $CH_3NH_3PbI_3$ perovskite solar cells due to elemental migration and chemical composition changes, Scientific reports 7 (1) (2017) 1–8.

[38] L. Wang, Q. Zhou, Z. Zhang, W. Li, X. Wang, Q. Tian, X. Yu, T. Sun, J. Wu, B. Zhang, A guide to use fluorinated aromatic bulky cations for stable and high-performance 2D/3D perovskite solar cells: The more fluorination the better?, Journal of Energy, Chemistry 64 (2022) 179–189.

[39] Y.J. Kang, S.I. Na, Multi-site passivation-based antisolvent additive engineering with gradient distribution for superior triple cation P-I-N perovskite solar cells, Nano Energy 97 (2022) 107193.

[40] Y. Xiao, L. Zhao, Y. Shi, N. Liu, Y. Liu, B. Liu, Q. Xu, C. He, X. Chen, Surface modification of 316L stainless steel by grafting methoxy poly(ethylene glycol) to improve the biocompatibility, Chemical Research in Chinese Universities 31 (4) (2015) 651–657.

[41] Z. Ren, K. Liu, H. Hu, X. Guo, Y. Gao, P.W.K. Fong, Q. Liang, H. Tang, J. Huang, H. Zhang, M. Qin, L. Cui, H.T. Chandran, D. Shen, M.F. Lo, A. Ng, C. Surya, M. Shao, C.S. Lee, X. Lu, F. Laquai, Y. Zhu, G. Li, Room-temperature multiple ligands-tailored SnO_2 quantum dots endow in situ dual-interface binding for upscaling efficient perovskite photovoltaics with high VOC, Light: Science & Applications. 10 (1) (2021) 239.

[42] C. Wang, X. Wang, Z. He, B. Zhou, D. Qu, Y. Wang, H. Hu, Q. Hu, Y. Tu, Minimizing voltage deficit in Methylammonium-Free perovskite solar cells via surface reconstruction, Chemical Engineering Journal 444 (2022), 136622.

[43] Z. Wu, J. Wu, S. Wang, C. Wang, Y. Du, Y. Wang, J. Geng, Y. Lin, W. Sun, Z. Lan, Multifunctional molecule of potassium nonafluoro-1-butanesulfonate for high-efficient perovskite solar cells, Chemical Engineering Journal 449 (2022), 137851.

[44] H.H. Fang, F. Wang, S. Adjokatse, N. Zhao, J. Even, M.A. Loi, Photoexcitation dynamics in solution-processed formamidinium lead iodide perovskite thin films for solar cell applications, Light: Science & Applications 5 (4) (2016) e16056.

[45] L. Zhu, X. Zhang, M. Li, X. Shang, K. Lei, B. Zhang, C. Chen, S. Zheng, H. Song, J. Chen, Trap state passivation by rational ligand molecule engineering toward efficient and stable perovskite solar cells exceeding 23% efficiency, Advanced Energy Materials 11 (20) (2021) 2100529.

[46] L. Yang, X. Ma, X. Shang, D. Gao, C. Wang, M. Li, C. Chen, B. Zhang, S. Xu, S. Zheng, Zwitterionic ionic liquid confer defect tolerance, high conductivity, and hydrophobicity toward efficient perovskite solar cells exceeding 22% efficiency, Solar RRL 5 (9) (2021) 2100352.

[47] T.H. Han, S. Tan, J. Xue, L. Meng, J.W. Lee, Y. Yang, Interface and defect engineering for metal halide perovskite optoelectronic devices, Advanced Materials 31 (47) (2019) 1803515.

[48] W. Chen, Y. Wu, J. Fan, A.B. Djurišić, F. Liu, H.W. Tam, A. Ng, C. Surya, W.K. Chan, D. Wang, Understanding the doping effect on NiO: toward high-performance inverted perovskite solar cells, Advanced Energy Materials 8 (19) (2018) 1703519.

[49] D. Shi, V. Adinolfi, R. Comin, M. Yuan, E. Alarousu, A. Buin, Y. Chen, S. Hoogland, A. Rothenberger, K. Katsiev, Low trap-state density and long carrier diffusion in organolead trihalide perovskite single crystals, Science 347 (6221) (2015) 519–522.

[50] P. You, G. Tang, J. Cao, D. Shen, T.W. Ng, Z. Hawash, N. Wang, C.-K. Liu, W. Lu, Q. Tai, 2D materials for conducting holes from grain boundaries in perovskite solar cells, Light: Science & Applications 10 (1) (2021) 1–12.

[51] Y.C. Zhao, W.K. Zhou, X. Zhou, K.H. Liu, D.P. Yu, Q. Zhao, Quantification of light-enhanced ionic transport in lead iodide perovskite thin films and its solar cell applications, Light: Science & Applications 6 (5) (2017) e16243.

[52] K.M. Kim, B.J. Choi, M.H. Lee, G.H. Kim, S.J. Song, J.Y. Seok, J.H. Yoon, S. Han, C. S. Hwang, A detailed understanding of the electronic bipolar resistance switching behavior in Pt/TiO_2/Pt structure, Nanotechnology 22 (25) (2011), 254010.

[53] T.X. Qin, E.M. You, M.X. Zhang, P. Zheng, X.F. Huang, S.Y. Ding, B.W. Mao, Z. Q. Tian, Quantification of electron accumulation at grain boundaries in perovskite polycrystalline films by correlative infrared-spectroscopic nanoimaging and Kelvin probe force microscopy, Light: Science & Applications. 10 (1) (2021) 84.